Organic Electronics 101 (2022) 106410

Contents lists available at ScienceDirect

Organic Electronics

journal homepage: www.elsevier.com/locate/orgel

Solution-processed bulk heterojunction broadband photodetectors based on perovskites incorporated with PbSe quantum dots

Baosen Zhang [a,1], Lening Shen [a,1], Luyao Zheng [a], Tao Zhu [a], Rui Chen [a], Lei Liu [a], Jie Zheng [b], Xiong Gong [a,*]

[a] School of Polymer Science and Polymer Engineering, College of Engineering and Polymer Science, The University of Akron, Akron, OH, 44325, USA
[b] Department of Chemical, Biomolecular and Corrosion Engineering, College of Engineering and Polymer Science, The University of Akron, Akron, OH, 44325, USA

ARTICLE INFO

Keywords:
Broadband photodetectors
Bulk heterojunction device structure
Perovskites
PbSe quantum Dots
Device performance

ABSTRACT

Broadband photodetectors (PDs) have great applications in both scientific and industrial sectors. In this study, we report room-temperature operated solution-processed bulk heterojunction (BHJ) broadband PDs based on perovskites incorporated with highly electrically conductive PbSe quantum dots (QDs). The p-type perovskites incorporated with the n-type PbSe QDs forming the BHJ composite thin film not only extend the spectral response up to the infrared region but also balance charge transport of the photoactive layer, resulting in boosted photocurrent and suppressed dark current, consequently, enhanced device performance of the broadband PDs. As a result, the solution-processed BHJ broadband PDs exhibit a responsibility of 10 mA/W, a detectivity of 10^{11} Jones (1 Jones = 1 cm · $Hz^{1/2}$/W), and a linear dynamic range of 53 dB in the spectral response ranging from 350 nm to 2500 nm, where the BHJ broadband PDs are operated at room temperature. These studies indicate that we provide a facile way to develop room-temperature operated solution-processed broadband PDs.

1. Introduction

Photodetectors (PDs) are the electronics that convert light signals into electrical signals [1]. PDs have many industrial and scientific applications including image sensing, communications, chemical detection, remote control, environmental sensing, day-/night-time surveillance [2–4]. Currently gallium nitride (GaN), silicon (Si), indium gallium arsenide (InGaAs), and mercury cadmium telluride (HgCdTe) were typically used to fabricate PDs and then integrate them to cover the spectral response from 300 nm to 2500 nm [5–8]. In general, the detectivities of GaN, Si, InGaAs, and HgCdTe-based PDs were in the range of ~10^{13}, ~10^{13}, ~$10^{12,}$ and ~10^{10} Jones (1 Jones = 1 cm · $Hz^{1/2}$/W), respectively. Particularly, to reach the detectivities of ~10^{12} and ~10^{10} Jones for the InGaAs and HgCdTe-based PDs, respectively, these devices were required to be operated at low temperatures, for example, 4.2 K. Such cryogenic condition certainly restricted their applications [1,9].

Various semiconductors, such as inorganic quantum dots (QDs), semiconducting organic/polymeric materials, two-dimensional (2D) materials, and perovskites have been extensively studied to develop PDs and these PDs based on these materials with decent detectivities have been reported [9–18]. Organic/polymer-based PDs have gained abundant attention due to their advanced features such as low cost, physical flexibility, and excellent optoelectronic properties. But it was still a challenge to realize polymer-based PDs with decent IR photoresponse because of their short exciton lifetime induced by the phonon-exciton recombination.[11.12] Moreover, due to the difficulties in large-scale and high throughput fabrication of inorganic QDs and 2D materials as well as the high gate (or drive) voltages required for the operation of PDs with a thin-film transistor (TFTs) device structure, the applications of the PDs based on inorganic QDs and 2D materials were extremely restricted. Perovskites have been demonstrated to be the alternatives for photodetection applications because of their excellent optoelectronic properties [19–35]. But perovskites typically exhibit the spectral response up to 800 nm. To extend spectral response, either polymers or perovskites incorporated with inorganic QDs have been developed to realize broadband PDs [9,10,12,13,17,18].

In the past years, we have reported various room-temperature (RT) operated broadband PDs based on either polymers or perovskites incorporated with inorganic QDs [9,12,13,36]. Even though these PDs

* Corresponding author. Tel.: 330 972 4982; fax: 330 972 3406.
E-mail address: xgong@uakron.edu (X. Gong).
[1] These authors are contributed equally.

https://doi.org/10.1016/j.orgel.2021.106410
Received 8 October 2021; Received in revised form 29 October 2021; Accepted 25 November 2021
Available online 3 December 2021

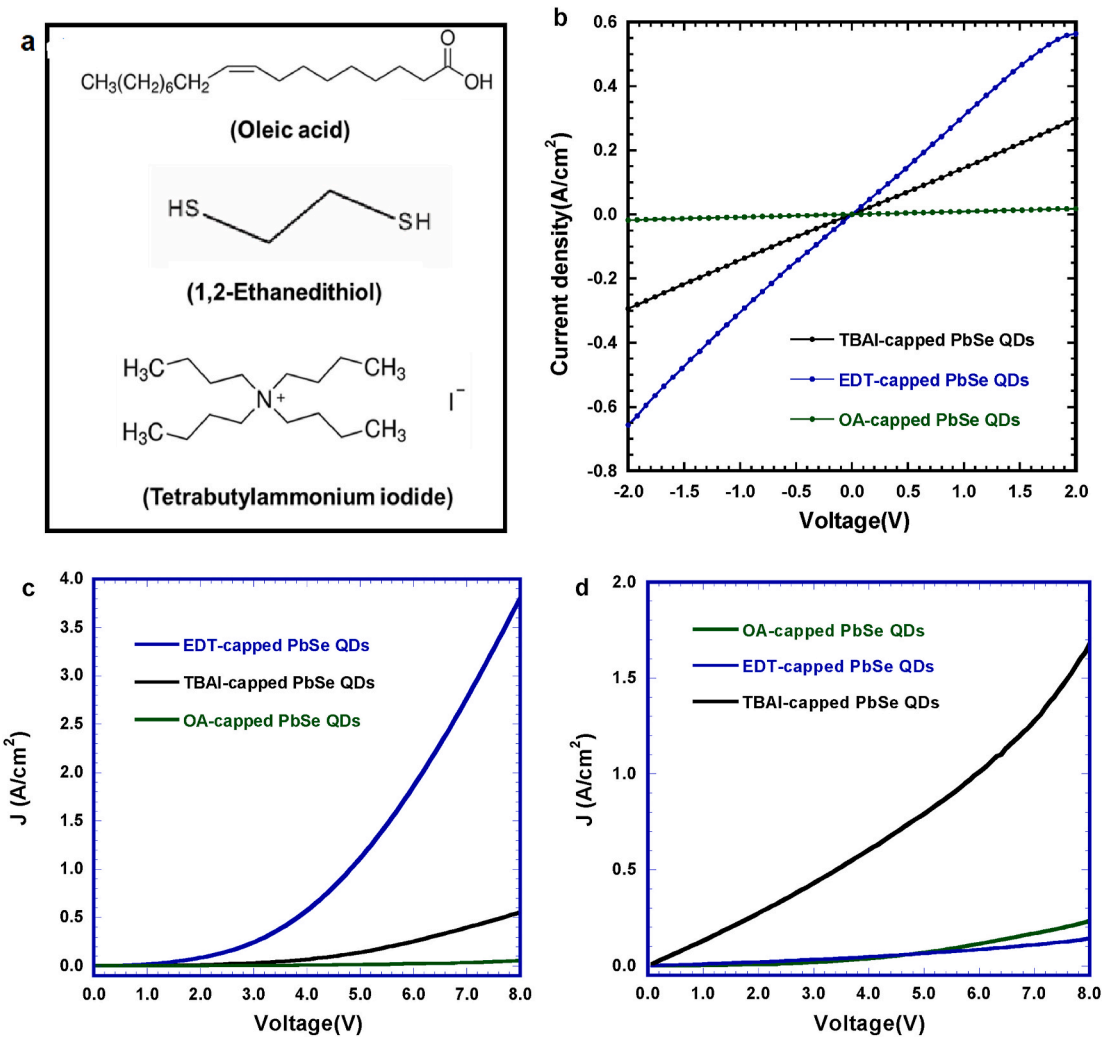

Fig. 1. (a) Molecular structures of oleic acid (OA), tetrabutylammonium iodide (TBAI) and 1,2-Ethanedithiol (EDT). (b) The electrical conductivities of the OA-capped PbSe QDs, the TBAI-capped PbSe QDs, the EDT capped PbSe QDs thin films. The J-V characterization of (c) the electron-only diodes and (d) the hole-only diodes based on the OA-capped PbSe QDs, the TBAI-capped PbSe QDs, and the EDT capped PbSe QDs thin films.

exhibited decent device performance, the photoactive layers were composed of multi-layer thin films, where inorganic QDs thin layer was deposited on the top of either polymers or perovskites layer. Such device architectures restricted the device performance of the broadband PDs [37]. Here, we report RT operated solution-processed bulk heterojunction (BHJ) broadband PDs based on perovskites mixed with highly electrically conductive PbSe QDs. The p-type perovskites incorporated with the n-type PbSe QDs forming BHJ composite single-layer thin film not only extend the spectral response up to the infrared region, but also balance charge transport, resulting in boosted photocurrent and suppressed dark current, consequently, enhanced device performance. As a result, the solution-processed BHJ broadband PDs exhibit a responsibility of 10 mA/W, a detectivity of 10^{11} Jones, and a linear dynamic range of 53 dB from the spectral response ranging from 350 nm to 2500 nm, where the broadband PDs are operated at room temperature.

2. Experimental

2.1. Materials

Oleic acid (OA), octadecene, lead oxide (PbO), selenium (Se), trioctylphosphine (TOP), diphenylphosphine (DPP), trabutylammonium iodide (TBAI), ethanedithiol (EDT), anhydrous octane, anhydrous hexane, methanol, ethanolamine, 2-methoxyethanol, acetonitrile (ACN) were purchased from Sigma-Aldrich. Zinc acetate (ZnAc) was purchased from Alfa Aesar [6,6].-phenyl-C_{61}-butyric acid methyl ester ($PC_{61}BM$) was purchased from Solenne BV. Poly(3,4-ethylenedioxythiophene): polystyrene sulfonate (PEDOT:PSS) was purchased from Heraeus Precious Metals North America. Lead iodide (PbI_2, 99.999%), anhydrous N,N-dimethylformamide (DMF), methylammonium iodide (MAI, CH_3NH_3I), ethanol, chlorobenzene (CB, 99.8%), bathocuproine (BCP, 99.99%) were purchased from Sigma-Aldrich. All materials are used as received without further purification.

2.2. Synthesis of PbSe QDs

The OA-capped PbSe QDs were synthesized by the hot injection method [38]. In brief, a given amount of Se was added in the TOP solution and then thermally hearted to 100 °C until Se was completely dispersed into the TOP solution. A 130 μL DPP solution was added to the above solution. PbO, octadecene, and OA were added into a flask under continuous stirring at 110 °C for 1 h in vacuum until PbO and OA were completely dissolved into octadecene. After that, the above solution was heated up to 180 °C. A Se solution was hot injected into the above PbO solution as quickly as possible. Within 5 min (min), the above-mixed solution was cooled down to room temperature. Afterward, 10 mL of hexane was injected into the above solution to generate an OA-capped PbSe QDs precursor solution. The OA-capped PbSe QDs solution was

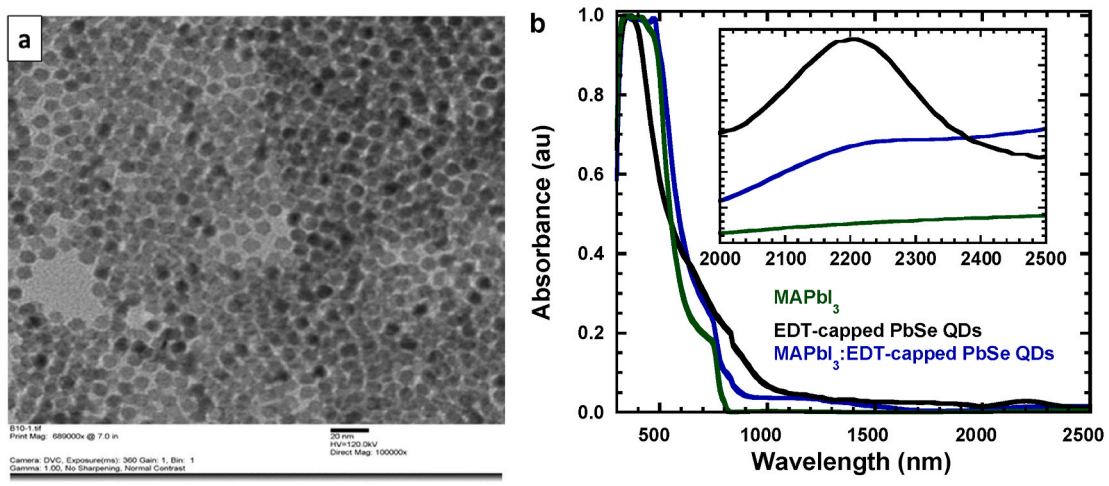

Fig. 2. (a) TEM image of the EDT-capped PbSe QDs thin film, (b) the absorption spectra of $MAPbI_3$ thin film, the EDT-capped PbSe QDs, the $MAPbI_3$: EDT-capped PbSe QDs BHJ composite thin film.

then precipitated and centrifuged for 15 min. After dumping the supernatant, 8 mL of hexane and then 8 mL of ethanol were frequently added to the above PbSe QDs solution and then centrifuged another 15 min. After it was dried in vacuum, the OA-capped PbSe QDs powder was finally produced. Finally, the OA-capped PbSe QDs were dispersed into octane making a 50 mg/mL solution for further applications. TBAI was dissolved into methanol and EDT was dissolved into acetonitrile to make their corresponding solutions. The OA-capped PbSe QDs thin film was spin-coated on the substrate with a spin speed of 2500 rpm for 30 s (s). Either TBAI or EDT solution was dropped on the top of the OA-capped PbSe QDs thin film for 1 min. Afterward, methanol was used to wash out the excess residue to generate either the TBAI-capped PbSe QDs or the EDT-capped PbSe QDs thin film. Finally, either the TBAI-capped PbSe QDs or the EDT-capped PbSe QDs were peeled off and then dispersed into octane making 50 mg/mL solution for further applications.

2.3. Preparation of $MAPbI_3$ and $MAPbI_3$:EDT-capped PbSe QDs BHJ composite thin films

$MAPbI_3$ thin film was prepared by a two-step method [39]. The $MAPbI_3$:EDT-capped PbSe QDs BHJ composite thin film was also prepared by a two-step method. After PbI_2 layer was spin-coated with a spin speed of 6000 rpm from PbI_2 solution, the OA-capped PbSe QDs thin film was deposited on the top of PbI_2 layer by the spin-coated with a spin speed of 2500 rpm for 30 s. Afterward, OA was substituted by EDT through the procedure described above. And then MAI was deposited on the top of the EDT-capped PbSe QDs thin film from MAI ethanol solution with a spin speed of 6000 rpm, followed with thermal annealing at 110 °C for 40 min to form the $MAPbI_3$:EDT-capped PbSe QDs BHJ composite thin film.

2.4. Characterization of thin films

The absorption spectra of thin films were measured by Lambda 750 UV/Vis/NIR spectrometer from PerkinElmer Company. The transmission electron microscopy (TEM) images were measured by Model JEOL JSM-1230. The film thickness was measured using a DektakXT surface profile measuring system. The electrical conductivities of thin films were measured using the Keithley model (2400) source measure unit in dark.

2.5. Fabrication and characterization of the BHJ broadband PDs

The pre-cleaned ITO-coated glass substrate was preheated before ~40 nm PEDOT:PSS thin layer was deposited by spin-cast method, and then followed with thermal annealing at 150 °C for 10 min. After that, the $MAPbI_3$:EDT-capped PbSe QDs BHJ composite thin film was deposited on the top of the PEDOT:PSS layer in the glove box with a nitrogen atmosphere. Then ~50 nm $PC_{61}BM$ was spin-coated on the top of the $MAPbI_3$: EDT-capped PbSe QDs BHJ composite thin film from $PC_{61}BM$ chlorobenzene solution. Then, ~9 nm thick BCP and ~110 nm thick aluminum (Al) were sequentially deposited in vacuum with a base pressure of 6×10^{-6} mbar. The active device area was measured to be 0.16 cm^2.

The current density versus voltage (J-V) characteristics of PDs was measured by using Keithley model 2400 source measure unit both in dark and under the monochromatic light at the wavelength (λ) of 500 nm with the light intensity of 0.28 mW/cm^2, 1300 nm with the light intensity of 0.10 mW/cm^2, and 2400 nm with the light intensity of 0.04 mW/cm^2, respectively. The external quantum efficiency (EQE) spectra were measured by a quantum efficiency measurement system (QEX10) with a 300 W steady-state xenon lamp as the source light. The transient photocurrent measurement was performed on a homemade setup by using an optical chopper controlled at λ of 532 nm laser pulse at a frequency of 2 kHz. The impedance spectra were measured by the HP 4194A impedance/gain-phase analyzer under one sun illumination, with an oscillating voltage of 50 mV and a frequency of 5 Hz–15 MHz, at open-circuit voltage conditions.

3. Results and discussion

Fig. 1a displays the molecular structures of OA, TBAI, and EDT. Among them, OA possesses the longest carbon-carbon chain and EDT has the shortest one, which implies that the EDT-capped PbSe QDs probably have the highest electrical conductivity among these three different PbSe QDs. To verify this hypothesis, the current density versus voltage characteristics of the OA-capped PbSe QDs, the TBAI-capped PbSe QDs, and the EDT-capped PbSe QDs thin films sandwiched by the same metal (Al) electrodes are investigated and the results are shown in Fig. 1b. The electrical conductivities of the OA-capped PbSe QDs, the TBAI-capped PbSe QDs, and the EDT-capped PbSe QDs thin films are estimated according to $\sigma = \frac{J}{V} \cdot l$ (where σ is the electrical conductivity (S/m), J is the current density (A/cm^2), V is the voltage, l is the thickness of the thin film (nm)). The electrical conductivity of the EDT-capped PbSe QDs thin film is higher than that of the TBAI-capped PbSe QDs thin film,

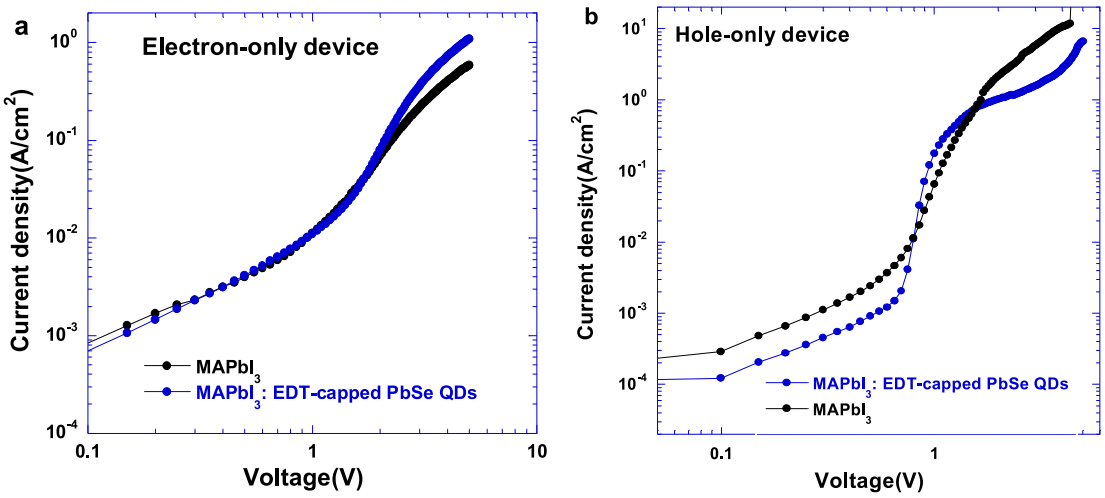

Fig. 3. The J-V characterization of (a) the electron-only diodes and (b) the hole-only diodes based on pristine $MAPbI_3$ thin film and the $MAPbI_3$:EDT-capped PbSe QDs BHJ composite thin film.

which is higher than that of the OA-capped PbSe QDs thin film.

The charge carrier mobilities of the OA-capped PbSe QDs, the TBAI-capped PbSe QDs, and the EDT-capped PbSe QDs thin films are further investigated using the space-charge-limited-current (SCLC) method based on the Mott-Gurney model [40,41]. Fig. 1c and d presents the current versus voltage (I–V) characteristics of the hole-only and electron-only diodes fabricated by different PbSe QDs thin films. The device structures of the electron-only and hole-only diodes are shown in Schemes S1 and S2. At low voltage, the I–V curve conforms the Ohm's law in the Ohmic region and the trap-filling region. The SCLC is described as $J = \frac{8}{9}\varepsilon_0\varepsilon\mu\frac{V^2}{L^3}$ (where μ is the charge mobility, V is the applied voltage and L is the thickness of the active layer, ε_0 is the permittivity of free space of 8.55×10^{-12} F m^{-1}, ε is the relative dielectric constant of the active layer, which is 21 F m^{-1}. [42]) The electron mobilities of the OA-capped PbSe QDs thin film, the TBAI-capped PbSe QDs thin film, and the EDT-capped PbSe QDs thin film are calculated to be 1.0×10^{-7}, 1.6×10^{-5}, and 1.2×10^{-4} cm^2/(Vs), respectively. Whereas the hole mobilities of the OA-capped PbSe QDs thin film, the TBAI-capped PbSe QDs thin film, and the EDT-capped PbSe QDs thin film are calculated to be 2.9×10^{-7}, 4.6×10^{-5}, 4.0×10^{-6} cm^2/(Vs), respectively. Thus, the OA-capped PbSe QDs thin film is a p-type semiconductor with poor charge carrier mobility. The charge carrier mobility of the TBAI-capped PbSe QDs thin film is enhanced compared to that of the OA-capped PbSe QDs thin film due to a short chain of TBAI with respect to OA. The charge carrier mobility of the EDT-capped PbSe QDs thin film is further boosted compared to that of the TBAI-capped PbSe QDs thin film since EDT molecular possesses a shorter carbon-carbon chain with respect to that of TBAI molecular. Moreover, the electron mobility (1.2×10^{-4} cm^2/(Vs)) is dramatically larger than the hole mobility (4.0×10^{-6} cm^2/(Vs)), which indicates that the EDT-capped PbSe QDs thin film is a n-type semiconductor.

Fig. 2a shows the transmission electron microscopy (TEM) image of the EDT-capped PbSe QDs thin film. Thus, the diameter of PbSe QDs is estimated to be ~8.5 nm and the distribution of the sizes of PbSe QDs is narrow. Moreover, based on the quantum confinement, the bandgap (E_g) is described as $Eg(QDs) = Eg(bulk) + \frac{\pi^2\hbar^2}{8R^2}\left(\frac{1}{m_e} + \frac{1}{m_h}\right)$, (where $E_g(bulk)$ is the bulk bandgap of QDs, n is the quantum number, h is the Planck constant, R is the size of QDs, m_e is the electron effective mass, m_h is the hole effective mass). If the effective electron mass is 0.05 m_0 and the effective hole mass is 0.04 m_0. The value of m_0 is 9.1×10^{-31} kg, the quantum number n is 1 and $E_g(bulk)$ of PbSe is 0.28 eV [41–50]. Thus, E_g of the EDT-capped PbSe QDs is calculated to be ~0.5 eV.

Fig. 2b shows the UV–visible absorption spectra of the EDT-capped PbSe QDs thin film, $MAPbI_3$ thin film, and the $MAPbI_3$:EDT-capped PbSe QDs BHJ composite thin film. Pristine $MAPbI_3$ thin film possesses absorption up to 780 nm, whereas the EDT-capped PbSe QDs thin film presents a wide absorption ranging from 300 nm to 2500 nm. Based on the cut-off of absorption, the optical gap of the EDT-capped PbSe QDs is estimated to be 0.5 eV, which is consistent with the value from the SEM results. Compared to $MAPbI_3$ thin film, the EDT-capped PbSe QDs thin film exhibits an absorption from the UV–visible to the near-infrared region, which could serve as a complementary absorber for $MAPbI_3$ thin film in the spectral range from 300 nm to 2500 nm.

It was reported that pristine $MAPbI_3$ is a p-type semiconductor. Thus the n-type EDT-capped PbSe QD is used to form the $MAPbI_3$:EDT-capped

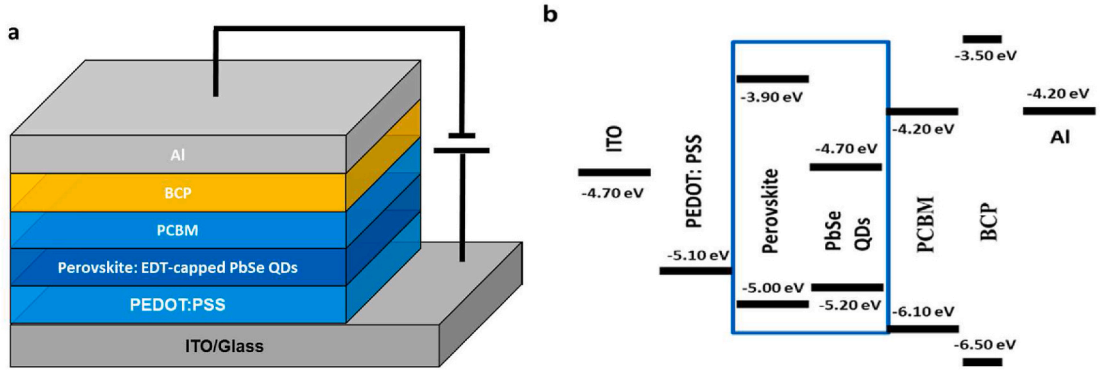

Scheme 1. (a) Device structure of the broadband PDs, and (b) the LUMO and HOMO energy levels of the materials used for the fabrication of the broadband PDs.

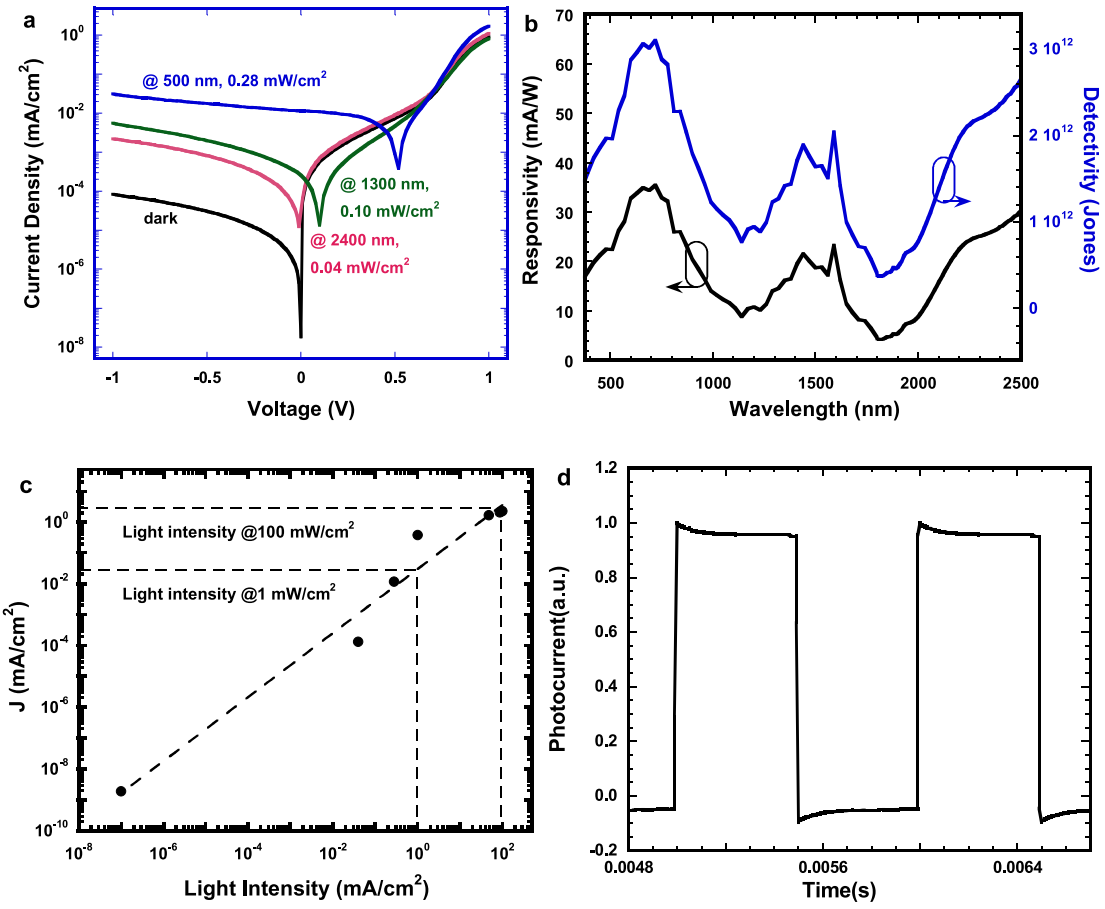

Fig. 4. (a) The J-V characteristics, (b) responsivity and detectivity, (c) the photocurrent versus the light intensity, and the response time of the BHJ broadband PDs based on the $MAPbI_3$:EDT-capped PbSe QDs BHJ composite thin film.

PbSe QDs BHJ composite thin film for balancing charge transport of the photoactive layer. To verify this hypothesis, the charge carrier mobilities of pristine $MAPbI_3$ thin film and the $MAPbI_3$:EDT-capped PbSe QDs BHJ composite thin film are further investigated using the SCLC method based on the Mott-Gurney model [40,41]. Fig. 3 presents the J-V characteristics of the electron-only diodes and the hole-only diodes based on pristine $MAPbI_3$ thin film and the $MAPbI_3$:EDT-capped PbSe QDs BHJ composite thin film. The device structures of the hole-only and the electron-only diodes are the same as those shown in Schemes S1 and S2, the active layers are either pristine $MAPbI_3$ or the $MAPbI_3$:EDT-capped PbSe QDs BHJ composite thin films. The electron and hole mobilities of pristine $MAPbI_3$ thin film are calculated to be 1.5×10^{-4} and 1.1×10^{-3} $cm^2/(Vs)$, respectively. These results are consistent with our previous studies and are in good agreement with other reports [51–53]. These results further indicate that pristine $MAPbI_3$ thin film is indeed a p-type semiconductor. The electron and hole mobilities of the $MAPbI_3$:EDT-capped PbSe QDs BHJ composite thin film are calculated to be 9.7×10^{-4} and 1.8×10^{-3} $cm^2/(Vs)$, respectively. Thus, the electron mobility of the $MAPbI_3$:EDT-capped PbSe QDs BHJ composite thin film is enhanced as compared to that of pristine $MAPbI_3$ thin film. Moreover, the charge transport of the $MAPbI_3$:EDT-capped PbSe QDs BHJ composite thin film is more balanced compared to that of pristine $MAPbI_3$ thin film. As a result, the broadband PDs based on the $MAPbI_3$:EDT--capped PbSe QDs BHJ composite thin film are expected to exhibit enhanced photocurrent.

The device structure of the BHJ broadband PDs is shown in Scheme 1a, where ITO acts as the anode, PEDOT:PSS is used as the hole extraction layer (HEL), $PC_{61}BM$ acts as the electron extraction layer (EEL), and the hole-block layer (HBL) as well, and BCP acts as an addition HBL, Al is aluminum and acts as the cathode, respectively. Scheme 1b displays the lowest unoccupied molecular orbital (LUMO) and highest occupied molecular orbital (HOMO) energy levels of $MAPbI_3$, the EDT-capped PbSe QDs, PCBM, and BCP, and the work functions of ITO, PEDOT:PSS, and Al electrodes. The LUMO offset between $MAPbI_3$, the EDT-capped PbSe QDs is 0.8 eV, which is larger than the exciton binding energy of $MAPbI_3$ [46,54], indicating that the separated electrons within the $MAPbI_3$:EDT-capped PbSe QDs BHJ composite thin film can be easily transported to the EDT-capped PbSe QDs electron acceptor layer and further collected by the Al cathode through the PCBM EET and the BCP HBL. Therefore, photo-induced charge transfer is expected to be occurred within the $MAPbI_3$:EDT-capped PbSe QDs BHJ composite thin film, resulting in enlarged photocurrent.

The J-V characteristics of the BHJ broadband PDs in dark and under the monochromatic light at a wavelength (λ) of 500 nm with the light intensity of is 0.28 mW/cm^2, λ of 1300 nm with the light intensity of 0.1 mW/cm^2 and λ of 2400 nm with the light intensity of 0.04 mW/cm^2 are shown in Fig. 4a. In dark, the BHJ broadband PDs exhibit the asymmetric J-V characteristics with the ratification ratios of 1.09×10^3 at $\pm$ 1 V, and 2.4×10^2 at $\pm$ 0.5 V, respectively. These results indicate that the BHJ broadband PDs possess excellent photodiode behaviors [55]. Different photocurrent densities observed from the BHJ broadband PDs under different monochromatic light illumination are ascribed to different light intensities, which indicate that the BHJ broadband PDs possess different photo responsibilities.

The responsivity (R) described as $R = J_{ph}/L_{ight}$ (where J_{ph} is the photocurrent density and L_{ight} is the light intensity) is often used to evaluate the device performance of PDs. Under a bias of −1 V, the BHJ

Table 1
Device performance of the BHJ Broadband PDs.

Photoactive layers	Wavelength (nm)	External bias (V)	J_{ph} (mA cm^{-2})	J_d (mA cm^{-2})	R (mA W^{-1})	D^* (Jones)
$MAPbI_3$: EDT-capped PbSe QDs	500	−0.1	1.23×10^{-2}	4.08×10^{-4}	43.93	3.84×10^{12}
	1300	−0.1	4.94×10^{-4}	4.08×10^{-4}	4.94	4.32×10^{11}
	2400	−0.1	1.09×10^{-4}	4.08×10^{-4}	2.73	2.39×10^{11}

broadband PDs exhibits R of 43.93 mA/W at λ of 500 nm, 4.94 mA/W at λ of 1300 nm, 2.73 mA/W at λ of 2400 nm, respectively.

If the dark current is only considered as the major contributor to the noise current, the project detectivity (D*) is described as $D* = R/\sqrt{2qJ_d}$ (where J_d is the dark current density, q is the elementary electric charge, $q = 1.6 \times 10^{-19}$ C, respectively) [11]. Thus, at RT, D* at λ of 500 nm, 1300 nm and 2400 nm are calculated to be 3.84×10^{12}, 4.32×10^{11}, 2.39×10^{11} Jones (1 Jones = 1 cm $Hz^{1/2}$/W), respectively, for the BHJ broadband PDs operated at a bias of −1 V. These D* values are compatible with the PDs based on InGaAs and 2D metal dichalcogenides. All these results certainly demonstrate that the BHJ broadband PDs exhibit high R and D*, indicating the BHJ broadband PDs have great potential applications.

Based on the external quantum efficiency (EQE) spectrum as shown in Fig. S1, and R and D* value at λ of 500 nm, 1300 nm, and 2400 nm for the BHJ broadband PDs, both R and D* values versus wavelength are speculated according to $R = EQE \times \frac{q}{h\nu} = EQE \times \frac{\lambda}{1240}$ and $D^* = R/\sqrt{(2qJ_d)}$. Fig. 4b presents R and D* versus wavelength for the BHJ broadband PDs. At RT, the BHJ broadband PDs exhibit over 10^{12} Jones detectivity and nearly over 10 mA/W responsibility from 350 nm to 2500 nm. Such decent R and D* over the broadband spectral region are ascribed to the $MAPbI_3$:EDT-capped PbSe QDs BHJ composite thin film. Table 1 summarizes the device performance of the BHJ broadband PDs.

The linear dynamic range (LDR) (the photosensitivity linearity) (typically quoted in dB), which is another device performance parameter used to evaluate PDs, is calculated according to the equation of LDR = 20 log (J^*_{ph}/J_d), where J^*_{ph} is the photocurrent measured at the light intensity of 1 mW/cm^2. Fig. 4c shows the photocurrent densities versus the incident light intensities of the BHJ broadband PDs. At RT, the LDR is 53 dB, which is compatible with that (66 dB, at 4.2K) from InGaAs PDs.

The response time is another important parameter used to evaluate the device performance of PDs. Fig. 4d presents the transient photocurrents of the BHJ broadband PDs. The rise time is defined as the time required for output signals to increase from 10% to 90% of saturated photocurrent. Similarly, the fall time is defined as the time required for the output signal to decrease from 90% to 10% of saturated photocurrent. A rise time of 2 μs and a fall time of 8 μs are observed from the BHJ broadband PDs. The response time is also compatible with those reported values from polymer-based PDs, and InGaAs-based PDs PDs.

4. Conclusions

In this study, we reported room-temperature operated solution-processed bulk heterojunction (BHJ) broadband PDs based on perovskites incorporated with highly electrically conductive PbSe quantum dots (QDs). To boost the device performance of the broadband PDs, the electrical conductivity of PbSe QDs was first tuned through the substitution of the insulating organic molecule with a long-carbon chain by the less insulating organic molecule with a short-carbon chain. It was found that the substitution not only can enhance the electrical conductivity but also can tune the intrinsic properties of PbSe QDs. Afterward, the p-type perovskites incorporated with the n-type PbSe QDs forming BHJ composite thin film were generated. This novel BHJ composite thin film not only possessed extended spectral response up to the infrared region but also exhibited balanced charge transport of the photoactive layer, which could boost the photocurrent and suppress the dark current, consequently, resulting in enhanced device performance. As a result, the solution processed BHJ broadband PDs exhibited a responsibility of 10 mA/W, a detectivity of 10^{11} Jones, and a linear dynamic range of 53 dB from the spectral response ranging from 350 nm to 2500 nm, where the PDs were operated at room temperature. Our studies indicated that we have provided a facile way to develop room-temperature operated solution-processed broadband PDs.

Declaration of competing interest

The authors declare that they have no known competing financial interests or personal relationships that could have appeared to influence the work reported in this paper.

Acknowledgment

We acknowledge National Science Foundation (EECS 1351785) for financial support.

Appendix A. Supplementary data

Supplementary data to this article can be found online at https://doi.org/10.1016/j.orgel.2021.106410.

References

[1] A.R. Jha, Infrared Technology: Application to Electrooptics, Photonic Devices, and Sensors, Wiley, New York, 2000.
[2] A. Rogalski, J. Antoszewski, L. Faraone, Third-generation infrared photodetector arrays, J. Appl. Phys. 105 (2009), 091101, https://doi.org/10.1063/1.3099572.
[3] E. Monroy, F. Omns, F. Calle, Wide-bandgap semiconductor ultraviolet photodetectors, Semicond. Sci. Technol. 18 (2003) R33–R51, https://doi.org/10.1088/0268-1242/18/4/201.
[4] B.M. Zhengyuan Xu, Sadler, Ultraviolet communications: potential and state-of-the-art, IEEE Commun. Mag. 46 (2008) 67–73, https://doi.org/10.1109/MCOM.2008.4511651.
[5] A. Rogalski, HgCdTe infrared detector material: history, status and outlook, Rep. Prog. Phys. 68 (2005) 2267–2336, https://doi.org/10.1088/0034-4885/68/10/R01.
[6] H. Tan, C. Fan, L. Ma, X. Zhang, P. Fan, Y. Yang, W. Hu, H. Zhou, X. Zhuang, X. Zhu, A. Pan, Single-crystalline InGaAs nanowires for room-temperature high-performance near-infrared photodetectors, Nano-Micro Lett. 8 (2016) 29–35, https://doi.org/10.1007/s40820-015-0058-0.
[7] X. Dai, S. Zhang, Z. Wang, G. Adamo, H. Liu, Y. Huang, C. Couteau, C. Soci, GaAs/AlGaAs nanowire photodetector, Nano Lett. 14 (2014) 2688–2693, https://doi.org/10.1021/nl5006004.
[8] S. Keuleyan, J. Kohler, P. Guyot-Sionnest, Photoluminescence of mid-infrared HgTe colloidal quantum dots, J. Phys. Chem. C 118 (2014) 2749–2753, https://doi.org/10.1021/jp409061g.
[9] C. Liu, K. Wang, P. Du, E. Wang, X. Gong, A.J. Heeger, Ultrasensitive solution-processed broad-band photodetectors using $CH_3NH_3PbI_3$ perovskite hybrids and PbS quantum dots as light harvesters, Nanoscale 7 (2015) 16460–16469, https://doi.org/10.1039/C5NR04575D.
[10] T. Zhu, Y. Yang, L. Zheng, L. Liu, M.L. Becker, X. Gong, Solution-processed flexible broadband photodetectors with solution-processed transparent polymeric electrode, Adv. Funct. Mater. 30 (2020) 1909487, https://doi.org/10.1002/adfm.201909487.
[11] X. Gong, M. Tong, Y. Xia, W. Cai, J.S. Moon, Y. Cao, G. Yu, C.-L. Shieh, B. Nilsson, A.J. Heeger, High-detectivity polymer photodetectors with spectral response from 300 nm to 1450 nm, Science 325 (2009) 1665–1667, https://doi.org/10.1126/science.1176706.
[12] W. Xu, H. Peng, T. Zhu, C. Yi, L. Liu, X. Gong, A solution-processed near-infrared polymer: PbS quantum dot photodetectors, RSC Adv. 7 (2017) 34633–34637, https://doi.org/10.1039/C7RA01199G.
[13] C. Liu, H. Peng, K. Wang, C. Wei, Z. Wang, X. Gong, PbS quantum dots-induced trap-assisted charge injection in perovskite photodetectors, Nanomater. Energy 30 (2016) 27–35, https://doi.org/10.1016/j.nanoen.2016.09.035.
[14] L. Zheng, W. Xu, X. Yao, T. Zhu, Y. Yang, L. Liu, X. Gong, Ultrasensitive and high gain solution-processed perovskite photodetectors by $CH_3NH_3PbI_{2.55}Br_{0.45}$: Zn_2SnO_4 bulk heterojunction composite, Emergent Mater 3 (2020) 1–7, https://doi.org/10.1007/s42247-020-00072-7.

[15] L. Zheng, K. Wang, T. Zhu, L. Liu, J. Zheng, X. Gong, Solution-processed ultrahigh detectivity photodetectors by hybrid perovskite incorporated with heterovalent neodymium cations, ACS Omega 4 (2019) 15873–15878, https://doi.org/10.1021/acsomega.9b01797.

[16] L. Zheng, T. Zhu, W. Xu, J. Zheng, L. Liu, X. Gong, Ultrasensitive perovskite photodetectors by Co partially substituted hybrid perovskite, ACS Sustain. Chem. Eng. 6 (2018) 12055–12060, https://doi.org/10.1021/acssuschemeng.8b02363.

[17] W. Xu, Y. Guo, X. Zhang, L. Zheng, T. Zhu, D. Zhao, W. Hu, X. Gong, Room-temperature-operated ultrasensitive broadband photodetectors by perovskite incorporated with conjugated polymer and single-wall carbon nanotubes, Adv. Funct. Mater. 28 (2018) 1705541, https://doi.org/10.1002/adfm.201705541.

[18] L. Zheng, T. Zhu, W. Xu, L. Liu, J. Zheng, X. Gong, F. Wudl, Solution-processed broadband polymer photodetectors with a spectral response of up to 2.5 μm by a low bandgap donor–acceptor conjugated copolymer, J. Mater. Chem. C. 6 (2018) 3634–3641, https://doi.org/10.1039/C8TC00437D.

[19] C. Xie, F. Yan, Perovskite/poly(3-hexylthiophene)/graphene multiheterojunction phototransistors with ultrahigh gain in broadband wavelength region, ACS Appl. Mater. Interfaces 9 (2017) 1569–1576, https://doi.org/10.1021/acsami.6b11631.

[20] S.H. Yu, Y. Lee, S.K. Jang, J. Kang, J. Jeon, C. Lee, J.Y. Lee, H. Kim, E. Hwang, S. Lee, J.H. Cho, Dye-sensitized MoS_2 photodetector with enhanced spectral photoresponse, ACS Nano 8 (2014) 8285–8291, https://doi.org/10.1021/nn502715h.

[21] R. Pan, H. Li, J. Wang, X. Jin, Q. Li, Z. Wu, J. Gou, Y. Jiang, Y. Song, High-responsivity photodetectors based on formamidinium lead halide perovskite quantum dot–graphene hybrid, Part. Part, Syst. Charact. 35 (2018) 1700304, https://doi.org/10.1002/ppsc.201700304.

[22] D.-H. Kang, S.R. Pae, J. Shim, G. Yoo, J. Jeon, J.W. Leem, J.S. Yu, S. Lee, B. Shin, J.-H. Park, An ultrahigh-performance photodetector based on a perovskite–transition-metal-dichalcogenide hybrid structure, Adv. Mater. 28 (2016) 7799–7806, https://doi.org/10.1002/adma.201600992.

[23] J. Lu, A. Carvalho, H. Liu, S.X. Lim, A.H. CastroNeto, C.H. Sow, Hybrid bilayer WSe2 _$CH3_NH3_PbI3_O$rganolead halide perovskite as a high -performancephotodetector, Angew. Chem. 128 (2016) 12124–12128, https://doi.org/10.1002/ange.201603557.

[24] M. He, Y. Chen, H. Liu, J. Wang, X. Fang, Z. Liang, Chemical decoration of $CH_3NH_3PbI_3$ perovskites with graphene oxides for photodetector applications, Chem. Commun. 51 (2015) 9659–9661, https://doi.org/10.1039/C5CC02282G.

[25] C. Ma, Y. Shi, W. Hu, M.-H. Chiu, Z. Liu, A. Bera, F. Li, H. Wang, L.-J. Li, T. Wu, Heterostructured $WS_2/CH_3NH_3PbI_3$ photoconductors with suppressed dark current and enhanced photodetectivity, Adv. Mater. 28 (2016) 3683–3689, https://doi.org/10.1002/adma.201600069.

[26] J. Han, J. Wang, Photodetectors based on two-dimensional materials and organic thin-film heterojunctions, Chin. Phys. B 28 (2019), 017103, https://doi.org/10.1088/1674-1056/28/1/017103.

[27] V.Q. Dang, G.-S. Han, T.Q. Trung, L.T. Duy, Y.-U. Jin, B.-U. Hwang, H.-S. Jung, N.-E. Lee, Methylammonium lead iodide perovskite-graphene hybrid channels in flexible broadband phototransistors, Carbon 105 (2016) 353–361, https://doi.org/10.1016/j.carbon.2016.04.060.

[28] G. Konstantatos, J. Clifford, L. Levina, E.H. Sargent, Sensitive solution-processed visible-wavelength photodetectors, Nat. Photonics 1 (2007) 531–534, https://doi.org/10.1038/nphoton.2007.147.

[29] J.Y. Kim, V. Adinolfi, B.R. Sutherland, O. Voznyy, S.J. Kwon, T.W. Kim, J. Kim, H. Ihee, K. Kemp, M. Adachi, M. Yuan, I. Kramer, D. Zhitomirsky, S. Hoogland, E. H. Sargent, Single-step fabrication of quantum funnels via centrifugal colloidal casting of nanoparticle films, Nat. Commun. 6 (2015) 7772, https://doi.org/10.1038/ncomms8772.

[30] J.P. Clifford, G. Konstantatos, K.W. Johnston, S. Hoogland, L. Levina, E.H. Sargent, Fast, sensitive and spectrally tuneable colloidal-quantum-dot photodetectors, Nat. Nanotechnol. 4 (2009) 40–44, https://doi.org/10.1038/nnano.2008.313.

[31] Y. Guo, C. Liu, H. Tanaka, E. Nakamura, Air-stable and solution-processable perovskite photodetectors for solar-blind UV and visible light, J. Phys. Chem. Lett. 6 (2015) 535–539, https://doi.org/10.1021/jz502717g.

[32] M. Ahmadi, T. Wu, B. Hu, A review on organic–inorganic halide perovskite photodetectors: device engineering and fundamental physics, Adv. Mater. 29 (2017), https://doi.org/10.1002/adma.201605242 n/a-n/a.

[33] C. Liu, H. Peng, K. Wang, C. Wei, Z. Wang, X. Gong, PbS quantum dots-induced trap-assisted charge injection in perovskite photodetectors, Nanomater. Energy 30 (2016) 27–35, https://doi.org/10.1016/j.nanoen.2016.09.035.

[34] C. Liu, K. Wang, P. Du, E. Wang, X. Gong, A.J. Heeger, Ultrasensitive solution-processed broad-band photodetectors using $CH_3NH_3PbI_3$ perovskite hybrids and PbS quantum dots as light harvesters, Nanoscale 7 (2015) 16460–16469, https://doi.org/10.1039/C5NR04575D.

[35] G. Konstantatos, L. Levina, J. Tang, E.H. Sargent, Sensitive solution-processed Bi_2S_3 nanocrystalline photodetectors, Nano Lett. 8 (2008) 4002–4006, https://doi.org/10.1021/nl802600z.

[36] T. Zhu, L. Zheng, X. Yao, L. Liu, F. Huang, Y. Cao, X. Gong, Ultrasensitive solution-processed broadband PbSe photodetectors through photomultiplication effect, ACS Appl. Mater. Interfaces (2019), https://doi.org/10.1021/acsami.8b21966.

[37] S. Yan, Q. Li, X. Zhang, S. Tang, W. Lei, J. Chen, A vertical structure photodetector based on all-inorganic perovskite quantum dots, J. Soc. Inf. Disp. 28 (2020) 9–15, https://doi.org/10.1002/jsid.853.

[38] C.-Y. Kuo, M.-S. Su, C.-S. Ku, S.-M. Wang, H.-Y. Lee, K.-H. Wei, Ligands affect the crystal structure and photovoltaic performance of thin films of PbSe quantum dots, J. Mater. Chem. 21 (2011) 11605–11612, https://doi.org/10.1039/C0JM04417B.

[39] J. Burschka, N. Pellet, S.-J. Moon, R. Humphry-Baker, P. Gao, M.K. Nazeeruddin, M. Grätzel, Sequential deposition as a route to high-performance perovskite-sensitized solar cells, Nature 499 (2013) 316–319, https://doi.org/10.1038/nature12340.

[40] H. Li, L. Duan, D. Zhang, Y. Qiu, Electric eield inside a hole-only device and insights into space-charge-limited current measurement for organic semiconductors, J. Phys. Chem. C 118 (2014) 9990–9995, https://doi.org/10.1021/jp5035618.

[41] M.A. Lampert, R.B. Schilling, Current Injection in Solids, Elsevier, 1970.

[42] I. Moreels, G. Allan, B. De Geyter, L. Wirtz, C. Delerue, Z. Hens, Dielectric function of colloidal lead chalcogenide quantum dots obtained by a Kramers-Krönig analysis of the absorbance spectrum, Phys. Rev. B 81 (2010), https://doi.org/10.1103/PhysRevB.81.235319.

[43] G. Zaiats, D. Yanover, R. Vaxenburg, J. Tilchin, A. Sashchiuk, E. Lifshitz, PbSe-based colloidal core/shell heterostructures for optoelectronic applications, Materials 7 (2014) 7243–7275, https://doi.org/10.3390/ma7117243.

[44] G. Allan, C. Delerue, Confinement effects in PbSe quantum wells and nanocrystals, Phys. Rev. B 70 (2004), https://doi.org/10.1103/PhysRevB.70.245321.

[45] A. Lipovskii, E. Kolobkova, V. Petrikov, I. Kang, A. Olkhovets, T. Krauss, M. Thomas, J. Silcox, F. Wise, Q. Shen, S. Kycia, Synthesis and characterization of PbSe quantum dots in phosphate glass, Appl. Phys. Lett. 71 (1997) 3406–3408, https://doi.org/10.1063/1.120349.

[46] Y. Zhang, Q. Dai, X. Li, J. Liang, Vicki.L. Colvin, Y. Wang, W.W. Yu, PbSe/CdSe and PbSe/CdSe/ZnSe hierarchical nanocrystals and their photoluminescence, Langmuir 27 (2011) 9583–9587, https://doi.org/10.1021/la201504d.

[47] A.C. Bartnik, F.W. Wise, A. Kigel, E. Lifshitz, Electronic structure of PbSe/PbS core-shell quantum dots, Phys. Rev. B 75 (2007), https://doi.org/10.1103/PhysRevB.75.245424.

[48] W.W. Yu, J.C. Falkner, B.S. Shih, V.L. Colvin, Preparation and characterization of monodisperse PbSe semiconductor nanocrystals in a noncoordinating solvent, Chem. Mater. 16 (2004) 3318–3322, https://doi.org/10.1021/cm049476y.

[49] B. De Geyter, Y. Justo, I. Moreels, K. Lambert, P.F. Smet, D. Van Thourhout, A. J. Houtepen, D. Grodzinska, C. de Mello Donega, A. Meijerink, D. Vanmaekelbergh, Z. Hens, The different nature of band edge absorption and emission in colloidal PbSe/CdSe core/shell quantum dots, ACS Nano 5 (2011) 58–66, https://doi.org/10.1021/nn102980e.

[50] A.I. Onyia, H.I. Ikeri, A.N. Nwobodo, Theoretical study of the quantum confinement effects on quantum dots using particle in a box model, Journal of Ovonic Research 14 (1) (2018) 49–54.

[51] Y. Chen, J. Peng, D. Su, X. Chen, Z. Liang, Efficient and balanced charge transport revealed in planar perovskite solar cells, ACS Appl. Mater. Interfaces 7 (2015) 4471–4475, https://doi.org/10.1021/acsami.5b00077.

[52] N. Ahn, D.-Y. Son, I.-H. Jang, S.M. Kang, M. Choi, N.-G. Park, Highly reproducible perovskite solar cells with average efficiency of 18.3% and best efficiency of 19.7% fabricated via Lewis base adduct of lead(II) iodide, J. Am. Chem. Soc. 137 (2015) 8696–8699, https://doi.org/10.1021/jacs.5b04930.

[53] W. Xu, L. Zheng, X. Zhang, Y. Cao, T. Meng, D. Wu, L. Liu, W. Hu, X. Gong, Efficient perovskite solar cells fabricated by Co partially substituted hybrid perovskite, Adv. Energy Mater. 8 (2018) 1703178, https://doi.org/10.1002/aenm.201703178.

[54] L.M. Herz, Charge-carrier dynamics in organic-inorganic metal halide perovskites, Annu. Rev. Phys. Chem. 67 (2016) 65–89, https://doi.org/10.1146/annurev-physchem-040215-112222.

[55] S.M. Sze, K.K. Ng, Physics of Semiconductor Devices, John Wiley & Sons, 2021.